UAVSAR Polarimetric Calibration

Alexander G. Fore, Bruce D. Chapman, Brian P. Hawkins, Scott Hensley, Cathleen E. Jones, Thierry R. Michel, and Ronald J. Muellerschoen

***Abstract*—UAVSAR is a reconfigurable, polarimetric L-band synthetic aperture radar (SAR) that operates in quad-polarization mode and is specifically designed to acquire airborne repeat track SAR data for interferometric measurements. In this paper, we present details of the UAVSAR radar performance, the radiometric calibration, and the polarimetric calibration. For the radiometric calibration we employ an array of trihedral corner reflectors as well as distributed targets. We show that UAVSAR is a well-calibrated SAR system for polarimetric applications, with absolute radiometric calibration bias better than 1 dB, residual root-mean-square (RMS) errors of ~ 0.7 dB, and RMS phase errors $\sim 5.3^\circ$. For the polarimetric calibration we have evaluated the methods of Quegan and Ainsworth et al. for cross-talk calibration and find that the method of Quegan gives cross-talk estimates that depend on target type while the method of Ainsworth et al. gives more stable cross-talk estimates. We find that both methods estimate leakage of the co-polarizations into the cross-polarizations to be in the order of -30 dB.**

I. Introduction

UNINHABITED Aerial Vehicle Synthetic Aperture Radar (UAVSAR) is a National Aeronautics and Space Administration (NASA) / Jet Propulsion Laboratory (JPL) L-band fully polarimetric SAR employing an electronically scanned array whose primary design goal is to enable robust repeat pass radar interferometric measurements of deforming surfaces either from natural or anthropogenic causes [1]. The radar is housed in a pod mounted to the fuselage of a Gulfstream III jet. Nominally, the aircraft flies at an altitude of 12.5 km and maps a 20 km swath with incidence angles ranging from 25° to 65°. The design of the radar results in single look complex (SLC) imagery with range and azimuth pixels spacing of 1.66 m and 1 m respectively. Electronic steering of the antenna is tied to the inertial navigation unit so that consistent pointing is achieved regardless of the platform yaw. The platform was modified to include a precision autopilot that allows the aircraft to fly a specified trajectory within a 5 m tube [2]. This enables UAVSAR platform to fly a series of flight lines with well prescribed interferometric baselines. Here we discuss the measured performance of the UAVSAR instrument, present the methods and results of the polarimetric calibration, and report the results of an evaluation of the instrument calibration stability during its first four years of operation.

II. Calibration Targets

We primarily use point targets for the radiometric and polarimetric calibration, in particular the Rosamond calibration array. On Rosamond dry lake in the Mojave Desert of California there is a permanent array of twenty-three 2.4 m trihedral corner reflectors that are used for radiometric and polarimetric calibration. These corner reflectors appear to the L-band radar as point targets and have a well-known impulse response, σ_{cr}, given by [3]

$$\sigma_{cr} = \frac{4\pi l^4}{\lambda^2} \begin{cases} \left(P_x + P_y + P_z - \frac{2}{P_x+P_y+P_z}\right)^2 & P_x + P_y \geq P_z \\ \left(\frac{P_x P_y}{P_x+P_y+P_z}\right)^2 & P_x + P_y \leq P_z \end{cases} \quad (1)$$

Here, $l = 2.4$ m is the length of each leg of the corner reflector[1], $\lambda = 0.2379$ m is the radar wavelength, and (P_x, P_y, P_z) are the components of the look vector, $\hat{P}$, decomposed into a rectangular coordinate system. This coordinate system has its origin where three short legs of the corner reflector meet and the ortha-normal axes are aligned with each of the three legs. Without loss of generality, we have chosen $P_x \leq P_y \leq P_z$ in the above equations.

The location of the corner reflector is determined by surveying its apex with precision Global Positioning System (GPS) processing. Ground motion due to seismic drift is accounted for by using the Plate Boundary Observatory GPS site near the town of Rosamond, CA. After removing systematic errors, the overall root-mean-square accuracy in range, including GPS platform positioning, is 3.7 cm.

III. SAR Performance

TABLE I
UAVSAR Radar Parameters

Parameter	Value
Frequency	1.26 GHz (0.2379 m)
Bandwidth	80 MHz
Polarization	Quad Polarization (4 channels)
Range Swath	20 km
Look Angle Range	$25^\circ - 65^\circ$
Antenna Size	0.5 m × 1.6 m
Transmit / Receive Array Size	4×12
Operating Altitude Range	2-18 km
Nominal Altitude	12.5 km

The UAVSAR instrument's performance has been evaluated in terms of the noise equivalent sigma zero (NESZ) and the resolution. In Table I we summarize the characteristics of the UAVSAR instrument and imaging geometry.

The authors are with the Jet Propulsion Laboratory, California Institute of Technology, Pasadena, CA 91109 USA (e-mail: Alexander.Fore@jpl.nasa.gov).

[1]To be clear, l is the shorter of the two possible linear dimensions of the corner reflector, the other being $\sqrt{2}l$, measured along the hypotenuse of each side.

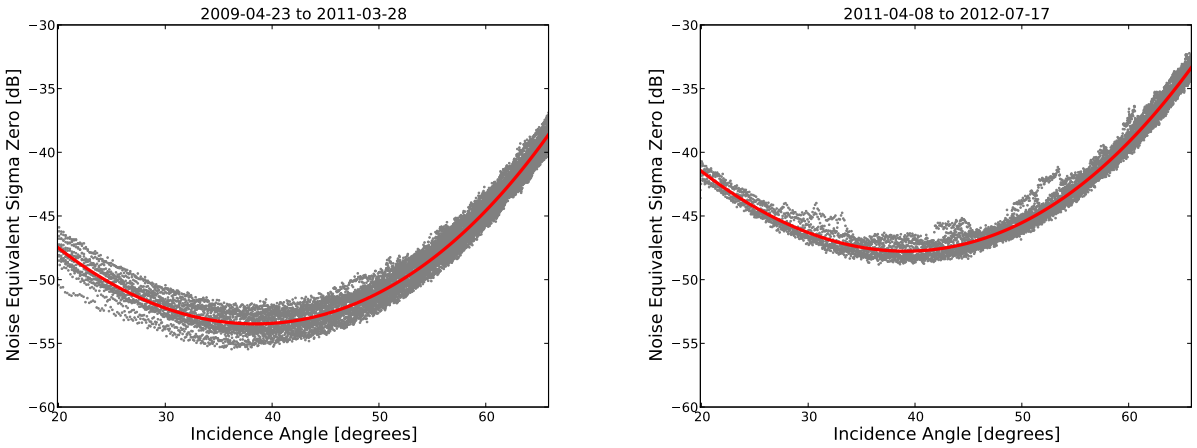

Fig. 1. (left) UAVSAR Noise equivalent sigma zero [dB] as a function of incidence angle for data collected before April 2011; (right) same for data collected after April 2011. In gray we plot the set of point-wise estimates from about 10 Rosamond data takes, and in red we plot a polynomial fit.

A. Noise Equivalent Sigma Zero

Roughly every two seconds, the UAVSAR radar skips the transmit pulse but continues to record data as usual. The power measured then is due to thermal noise of the radar and scene brightness temperature. If we process this noise energy in the same way as nominal radar echoes we obtain the radar cross section corresponding to the noise only energy, which is the noise equivalent sigma zero (NESZ). The NESZ provides a convient metric to asses the magnitude of a measured radar cross-section as compared to the instrinsic system noise.

In Figure 1 we plot the NESZ obtained from 10 Rosamond data takes as grey dots. We then perform a polynomial fit to these data to compute the average NESZ as a function of incidence angle to obtain the red line in Figure 1. We have observed two regimes in the NESZ performance over the current lifetime of the UAVSAR instrument, one pertaining to data collected before April 2011 (left) and another for that collected after April 2011 (right). The main difference is an increase in NESZ of ~ 5 dB due to a decrease in received power. The reason for this change in calibration is due to a change in hardware components, specifically the antenna.

B. SAR Resolution

We assess the geometric performance of the instrument by the observed spatial resolution of corner reflectors using data collected over the Rosamond calibration site. For each corner reflector imaged, we compute the full width at half maximum (FWHM) of the observed response, σ_0, in the range and azimuth directions. In Figure 2 we plot the average FWHM of all corner reflectors imaged on each Rosamond flight as a function of time. We see that the range and azimuth FWHM of the corner reflectors has been extremely stable over time, with an overall average of 2.53 to 2.54 m for the range resolution, and 0.941 m for the azimuth resolution. The standard deviation (STD) of all corner reflectors imaged is 4 cm for range resolution and 5.1 cm (HH) and 2.6 cm (VV) for azimuth resolution.

UAVSAR has a transmit bandwidth of 80 MHz and uses a cosine on pedestal weighting with $\eta = 0.5$, giving a broadening factor of 1.19 [4], allowing a theoretical range resolution of 2.23 m. Operational UAVSAR data is processed to an azimuth resolution of 1 m, thus the observed resolution and expected resolution are within 0.06 m for azimuth and within 0.3 m for range.

IV. Radiometric and Polarimetric Phase Calibration

Our calibration methodology is to perform radiometric and phase calibration during the image focusing process and to perform cross-talk calibration as a stand-alone process after the phase and radiometric calibration has been applied. This two step approach neglects cross-talk in the radiometric and phase calibration, however, the effect of cross-talk on the co-polarizations is negligible and we only use the co-polarization for the gain and co-polarization phase calibration estimation. We do use the cross-polarizations for the initial cross-polarization calibration, however, this calibration is performed again as part of the cross-talk calibration.

The processor computes a radiometric and phase adjustment as a function of antenna steering so that we only need to consider a single radiometric and phase calibration, independent of antenna steering in this work. The radiometric and phase calibration parameters are determined *a priori* using the corner reflector array described in Section II, and distributed target returns collected over agricultural fields in California's Central Valley. The flights are requested periodically to monitor the instrument calibration stability. Calibration data acquired in June 2011 (56 corner reflector observations) and November 2011 (181 corner reflector observations) were used in the calibration reported here.

A. Polarimetric Calibration Model

Here we discuss the derivation of the calibration parameters from observations. We denote the polarimetric backscatter

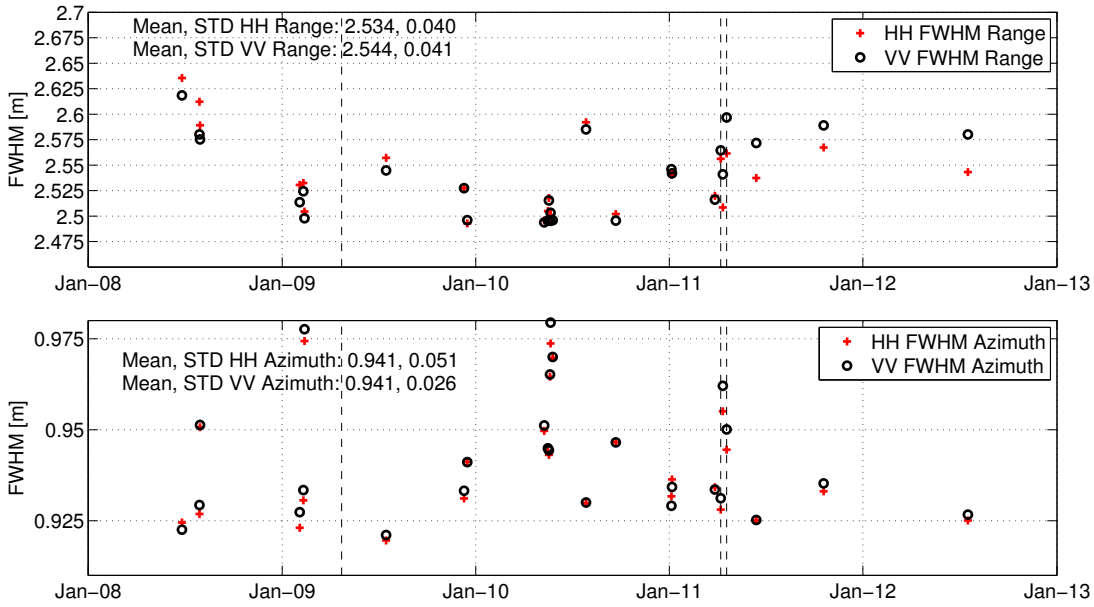

Fig. 2. (top) Average full width at half maximum in range resolution for all corner reflectors imaged on a given flight, plotted as a function of time over the UAVSAR mission to date (black VV polarization, red HH polarization); (bottom) same for the azimuth dimension. The dashed lines indicate changes in the calibration. Both the range and azimuth resolution have been very stable, with overall standard deviation of 4 cm for the range resolution and 2 to 5 cm for azimuth.

from a target by a complex scattering matrix, $\mathcal{S}$,

$$\mathcal{S} = \begin{bmatrix} s_{vv} & s_{vh} \\ s_{hv} & s_{hh} \end{bmatrix}, \tag{2}$$

where the notation s_{tr} indicates the transmitted polarization, t, and received polarization, r, of the radiation. After correcting for the antenna pattern and neglecting cross-talk, the measured signal, $\mathcal{S}^{'}$, which includes normalization and phase differences between the different polarization channels on both transmit and receive, can be related to $\mathcal{S}$ using calibration parameters as [5]–[9]

$$\mathcal{S}^{'} = A \begin{bmatrix} s_{vv} f^2 e^{i(\phi_{t,v}+\phi_{r,v})} & s_{vh}(f/g) e^{i(\phi_{t,h}+\phi_{r,v})} \\ s_{hv} f g e^{i(\phi_{t,v}+\phi_{r,h})} & s_{hh} e^{i(\phi_{t,h}+\phi_{r,h})} \end{bmatrix}. \tag{3}$$

Here, A is the absolute calibration constant, f is the co-polarization channel imbalance, g is the cross-polarization channel imbalance, $\phi_{t,j}$ is the phase error incurrent when transmitting polarization j, and $\phi_{r,j}$ is that for receiving polarization j. After absorbing an arbitrary phase into the overall calibration constant, A, this expression simplifies to

$$\mathcal{S}^{'} = A \begin{bmatrix} s_{vv} f^2 \exp i\,(\phi_t + \phi_r) & s_{vh}(f/g) \exp i\phi_r \\ s_{hv} f g \exp i\phi_t & s_{hh} \end{bmatrix} \tag{4}$$

where $\phi_t \equiv \phi_{t,v} - \phi_{t,h}$ and $\phi_r \equiv \phi_{r,v} - \phi_{r,h}$.

B. Estimation of Calibration Parameters

Here we outline the estimation of the calibration parameters ϕ_t, ϕ_r, A, f, and g using corner reflectors and distributed targets. We use point target data to estimate the co-polarized parameters A, f, and $\phi_t + \phi_r$ and distributed target data to estimate the cross-polarized parameters g and $\phi_t - \phi_r$.

The scattering matrix for a trihedral corner reflector is of the form [6], [7]

$$\mathcal{S}_{cr} = \sqrt{\sigma_{cr}} \begin{bmatrix} 1 & 0 \\ 0 & 1 \end{bmatrix}, \tag{5}$$

where σ_{cr} is given by Eq. 1. Combining (4) and (5), the measured scattering matrix for a trihedral corner reflector has the form

$$\mathcal{S}^{'}_{cr} = A\sqrt{\sigma_{cr}} \begin{bmatrix} f^2 \exp i\,(\phi_t + \phi_r) & 0 \\ 0 & 1 \end{bmatrix}. \tag{6}$$

As an example, we consider the corner reflector data shown in Figure 3, which has been calibrated to account only for range, area, and complex antenna gain variations within the antenna pattern. We plot the over-sampled radar cross-section (RCS) $s^{'}_{hh}s^{'*}_{hh}$ and $s^{'}_{vv}s^{'*}_{vv}$ (top left), the ratio of the over-sampled RCS to the predicted RCS from (1) in dB (top right), the measured phase bias of the HH channel's signal relative to the VV channel's signal (bottom left), and the co-channel imbalance (bottom right). Inset into the top right plot we compute the average ratio for all corner reflectors in dB and the root-mean-square-error (RMSE) of the ratio in natural units [2]. The text in the lower-left plot shows the overall bias and RMS values of the HH-VV phase, and in the bottom right we compute the bias and RMS of the co-polarization channel imbalance. We see that the observed corner reflector response is greater than predicted by 20.8 dB for the HH channel, 23.9 dB for the VV channel, the HH-VV phase difference is 38.5°, and the VV channel's signal is generally larger than that of the HH channel by as large a factor as 3 dB.

[2]We compute the root-mean-square of $\left(\sigma_0^{meas}/\sigma_0^{model} - 1\right)$.

We perform a linear fit of the residual measured RCS minus predicted RCS versus incidence angle, which gives the parameter A in (6) as a function of incidence angle as

$$A\left(\theta'\right) = A_0 + A_1\theta', \tag{7}$$

where $\theta' = \theta - 45°$.[3] We also derive f, the co-channel imbalance, from (6) as

$$f = \left[s'_{vv}s'^{*}_{vv} / \left(s'_{hh}s'^{*}_{hh}\right)\right]^{1/4}, \tag{8}$$

evaluated at the peak of the over-sampled corner reflector responses.

The phase bias between the HH and VV channels, estimated as the argument of $s'_{vv}s'^{*}_{hh}$, is plotted at the bottom left of Figure 3. We perform a 3rd order polynomial fit of the HH-VV phase error to the following model to obtain the estimate of $\phi_t + \phi_r$ as a function of incidence angle

$$\phi_t + \phi_r = a_{\phi_t+\phi_r} + b_{\phi_t+\phi_r}\theta' + c_{\phi_t+\phi_r}\theta'^2 + d_{\phi_t+\phi_r}\theta'^3. \tag{9}$$

We observe a linear trend of decreasing phase with increasing incidence angle. We perform a least-squares fit of the data to the model (9) to obtain an estimate of the co-polarization phase calibration parameters.

To determine the cross-polarization channel imbalance, we compute the average HV and VH radar return power over a large number of pixels using data collected along a 220 km flight line over the San Joaquin Valley. From (4), we estimate the cross-polarization imbalance as

$$g = \left(\frac{< |s'_{hv}|^2 >}{< |s'_{vh}|^2 >}\right)^{1/4}, \tag{10}$$

where $< \cdot >$ indicates a coherent average over the pixels. From reciprocity we expect $s_{hv} = s_{vh}$, so we estimate the cross-polarization phase bias as $\phi_t - \phi_r = \arg(< s'_{hv}s'^{*}_{vh} >)$. This average is made over the entire image, which is on the order of 10^9 pixels.

Finally, each UAVSAR data product has an associated annotation file, which contains the radiometric and phase calibration parameters. The relationship between the values stored in the annotation file and the parameters derived above is shown in Table II. Note that all of these keywords in the UAVSAR annotation files have LRTI80 appended.

TABLE II
THE RADIOMETRIC AND PHASE CALIBRATION PARAMETERS CONTAINED IN THE UAVSAR ANNOTATION FILE AND THEIR RELATIONSHIP TO THE PARAMETERS IN (1).

Sigma Nought Bias HH	$1/A$
Sigma Nought Bias HV	$1/(Afg)$
Sigma Nought Bias VH	$g/(Af)$
Sigma Nought Bias VV	$1/\left(Af^2\right)$
Sigma Nought Bias Slope HH	$-A_1/A_0^2$
Sigma Nought Bias Slope HV	$-A_1/\left(A_0^2 fg\right)$
Sigma Nought Bias Slope VH	$-A_1 g/\left(A_0^2 f\right)$
Sigma Nought Bias Slope VV	$-A_1/\left(A_0^2 f^2\right)$
HH-VV Phase Bias	$a_{\phi_t+\phi_r}$
HV-VH Phase Bias	$\phi_t - \phi_r$
HH-VV Phase Slope	$b_{\phi_t+\phi_r}$
HV-VH Phase Slope	0
HH-VV Phase Acceleration	$c_{\phi_t+\phi_r}$
HV-VH Phase Acceleration	0
HH-VV Phase Jerk	$d_{\phi_t+\phi_r}$
HV-VH Phase Jerk	0

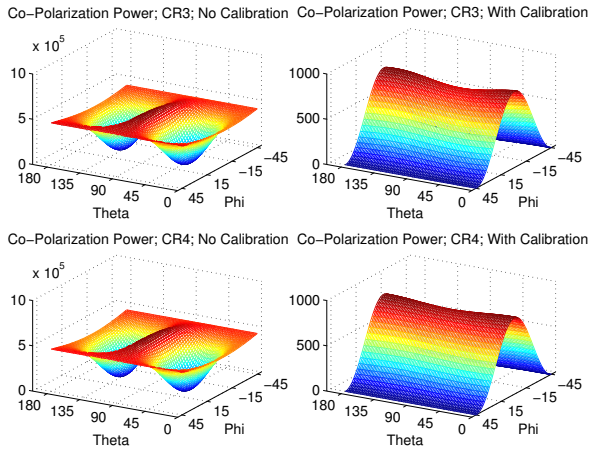

Fig. 5. (left) Co-polarization signature of two different corner reflectors (top and bottom) with only range, area, and antenna pattern calibration applied, (right) Co-polarization signatures of the same corner reflectors after radiometric and phase calibration. The double-peaked nature of the uncalibrated polarization signatures is due to the nearly 180° phase offset between the HH and VV channels, which makes the uncalibrated signatures look like those of a dihedral rather than a trihedral corner reflector.

C. Quality of the Polarimetric Calibration

Using the calibration parameters derived by the procedure described above, we reprocess the UAVSAR data acquired over the Rosamond corner reflector array to estimate the quality of the calibration. In Figure 4 we show a typical plot of the calibrated data. We find that the average ratio between the observed RCS and the model is a few hundredths of a dB, the RMSE of the ratio is 0.12 for HH and 0.11 for VV (0.49 dB and 0.45 dB respectively), the bias for the HH-VV phase is hundredths of a degree, RMS phase is 6°, and the co-channel imbalance RMS is 0.031.

On the left column of Figure 5 we plot the co-polarization signatures [10]–[12] of two trihedral corner reflectors with only range, area, and antenna pattern calibration and in the right column we plot the polarization signatures of the same corner reflectors after applying the phase and radiometric calibration parameters. Before radiometric and phase calibration the polarization signatures have a double-peaked nature. This is due to the nearly 180° phase offset between the HH and VV channels. After radiometric and phase calibration, the polarization signatures are similar to the ideal polarization signature for a trihedral corner reflector [10]–[12].

D. Temporal Stability of the Calibration Parameters

The calibration parameters are checked periodically for validity using data acquired in re-flights over the Rosamond corner reflector array. In Figure 6 we plot the RCS bias (top plot) RMS (second from the top) for HH (red) and VV (black),

[3]Note that 45° is the mounting angle of the UAVSAR antenna.

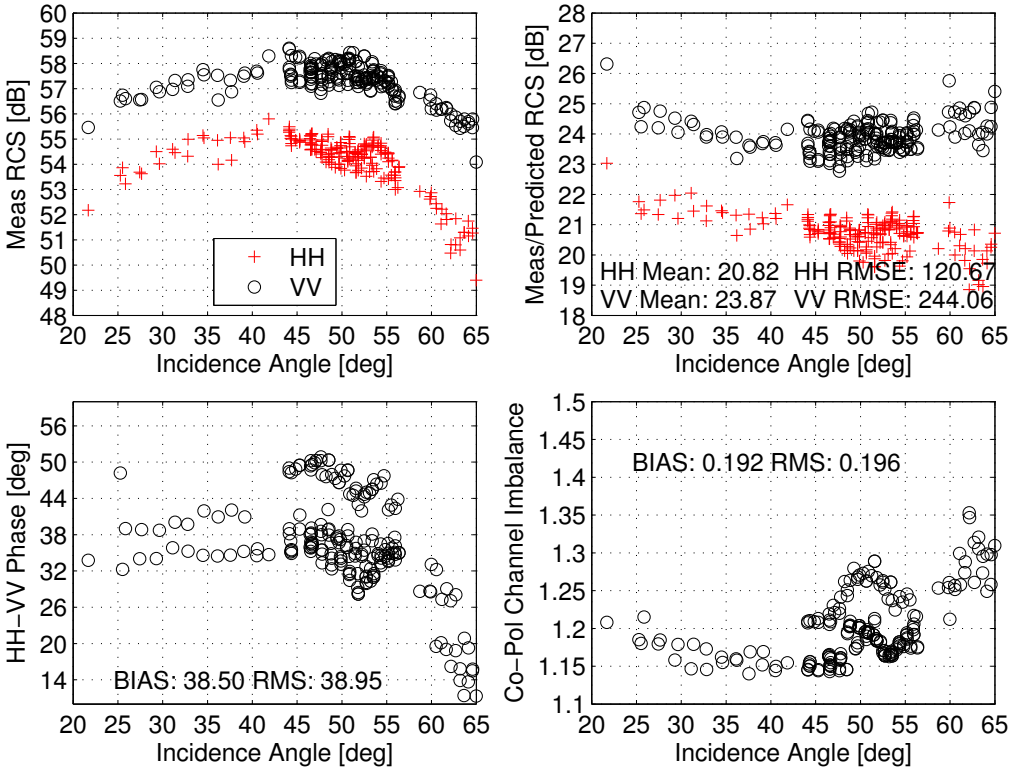

Fig. 3. UAVSAR data acquired over the Rosamond corner reflector array, from which we estimate the radiometric and phase calibration parameters A, $\phi_t + \phi_r$, and f. We plot the uncalibrated, over-sampled corner reflector response [dB] (top left), absolute calibration error [dB] (top right), the HH-VV phase bias [°] (bottom left), and co-channel imbalance (bottom right). Note the inset bias and RMS numbers have the same units as the y-axis for each plot.

and the HH-VV phase RMS (second from bottom) and co-polarization channel imbalance (bottom) as a function of time. We see that there are no overall trends in any of the error metrics computed with respect to the corner reflectors. The RCS RMS is nearly always less than 0.25 (corresponds to 0.97 dB) and the HH-VV phase RMS is nearly always less than $10°$.

V. Cross-Talk Calibration

Using the calibration procedure presented in Section IV-B, the UAVSAR data processor produces SLC data that are radiometrically and phase calibrated, but which do not have any residual cross-talk signal removed. We use this partially calibrated data as the input to the cross-talk calibration software. This provides a simple way to exclude cross-talk calibration while still maintaining radiometric and phase calibration, if desired. We have evaluated the models of Quegan [9] and Ainsworth et al. [8] by looking at the residuals after cross-talk removal. The discussion of these models and their efficacy at cross-talk removal in UAVSAR data is given below, with a detailed description of our implementation of the models in Appendix A.

A. Cross-Talk Model

We use the distortion models of Quegan [9] and Ainsworth et al. [8] to relate our observed scattering matrix elements (vector O) to the actual scattering matrix elements (vector S),

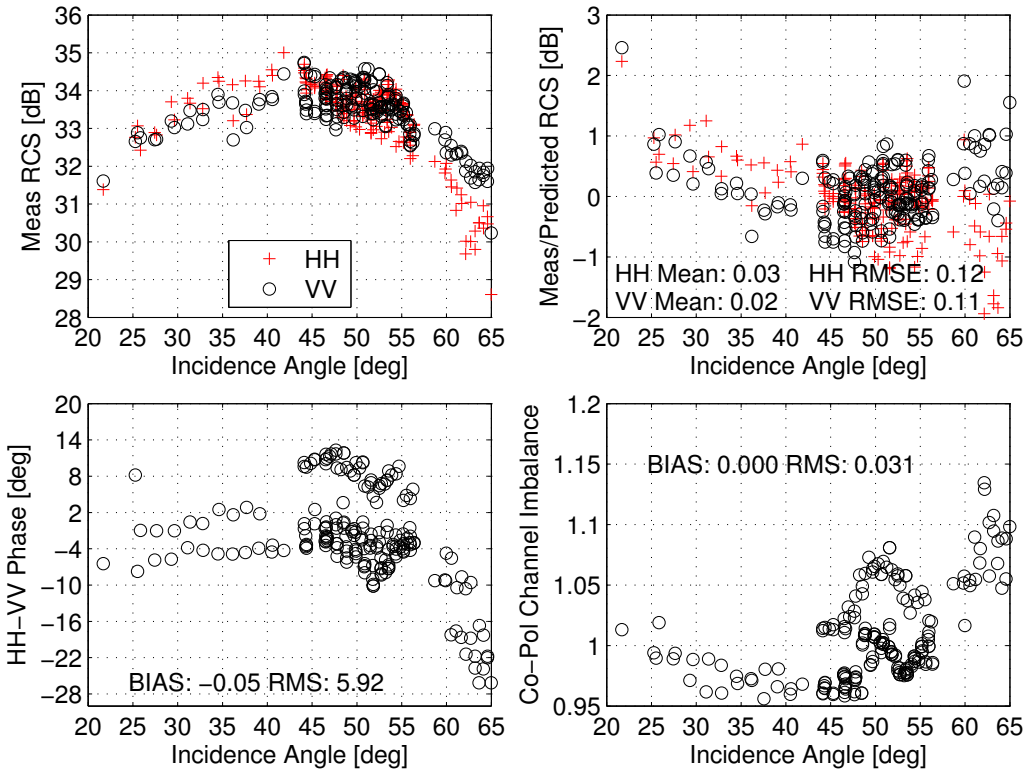

Fig. 4. UAVSAR data from Figure 3 after calibration. We see that the RMS error of the observed model ratio RCS is 0.12 (0.49 dB) for HH and 0.11 (0.45 dB) for VV, the HH-VV phase RMS error is 5.92°, and the co-polarization channel imbalance RMS error is 0.031. Note that only data with incidence angle less than 50° was used in these statistics. Note the inset bias and RMS numbers have the same units as the y-axis for each plot.

$$\begin{pmatrix} O_{hh} \\ O_{vh} \\ O_{hv} \\ O_{vv} \end{pmatrix} = Y \begin{pmatrix} 1 & w & v & vw \\ u & 1 & uv & v \\ z & wz & 1 & w \\ uz & z & u & 1 \end{pmatrix} \begin{pmatrix} \alpha k^2 & 0 & 0 & 0 \\ 0 & \alpha k & 0 & 0 \\ 0 & 0 & k & 0 \\ 0 & 0 & 0 & 1 \end{pmatrix} \begin{pmatrix} S_{hh} \\ S_{vh} \\ S_{hv} \\ S_{vv} \end{pmatrix} + \begin{pmatrix} N_{hh} \\ N_{vh} \\ N_{hv} \\ N_{vv} \end{pmatrix} \quad (11)$$

Here, Y is a complex number representing the absolute gain calibration, (u, v, w, z) are the complex cross-talk parameters (assumed to be small compared to 1), (k, α) are the co-polarization channel imbalance and cross-polarization channel imbalance respectively (assumed to be on the order of 1), and $\vec{N}$ represents noise.

We estimate the calibration parameters from distributed targets using methods described in [8], [9]. We simplify this distortion model with the assumption that the data is already calibrated for radiometric and co-polarization channel imbalance, as described in Section (IV). Thus we set $Y = 1$ and $k = 1/\sqrt{\alpha}$, and the system model then takes the form

$$\begin{pmatrix} O_{hh} \\ O_{vh} \\ O_{hv} \\ O_{vv} \end{pmatrix} = \mathbf{D} \begin{pmatrix} S_{hh} \\ S_{vh} \\ S_{hv} \\ S_{vv} \end{pmatrix} + \begin{pmatrix} N_{hh} \\ N_{vh} \\ N_{hv} \\ N_{vv} \end{pmatrix}, \quad (12)$$

where

$$\mathbf{D} = \begin{pmatrix} 1 & w\sqrt{\alpha} & v/\sqrt{\alpha} & vw \\ u & \sqrt{\alpha} & uv/\sqrt{\alpha} & v \\ z & wz\sqrt{\alpha} & 1/\sqrt{\alpha} & w \\ uz & z\sqrt{\alpha} & u/\sqrt{\alpha} & 1 \end{pmatrix} \quad (13)$$

is the distortion matrix. This system of equations has the solution

$$\begin{pmatrix} S_{hh} \\ S_{vh} \\ S_{hv} \\ S_{vv} \end{pmatrix} = \mathbf{\Sigma} \left[\begin{pmatrix} O_{hh} \\ O_{vh} \\ O_{hv} \\ O_{vv} \end{pmatrix} - \begin{pmatrix} N_{hh} \\ N_{vh} \\ N_{hv} \\ N_{vv} \end{pmatrix} \right], \quad (14)$$

where

$$\mathbf{\Sigma} = \begin{pmatrix} 1 & -w & -v & vw \\ -u/\sqrt{\alpha} & 1/\sqrt{\alpha} & uv/\sqrt{\alpha} & -v/\sqrt{\alpha} \\ -z\sqrt{\alpha} & wz\sqrt{\alpha} & \sqrt{\alpha} & -w\sqrt{\alpha} \\ uz & -z & -u & 1 \end{pmatrix} \times \frac{1}{(uw-1)(vz-1)} \quad (15)$$

is the calibration matrix.

B. Cross-Talk Estimation

We have used both the Quegan and the Ainsworth et al. methods of estimating the cross-talk parameters using distributed targets. In Appendix A we discuss the details of how

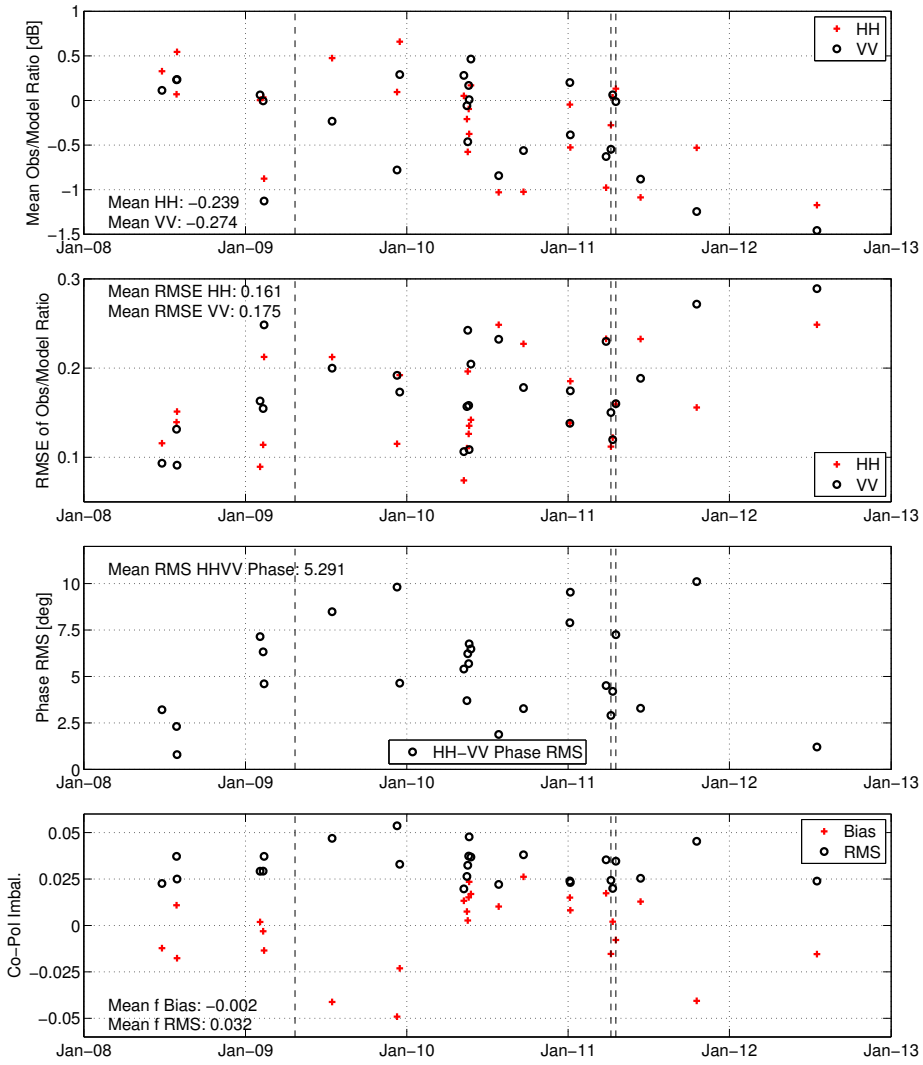

Fig. 6. RCS bias (top), RCS RMS error (2nd from top), HH-VV phase RMS (2nd from bottom), and Co-polarization imbalance bias and RMS (bottom) for all Rosamond flight lines as a function of time. Each point represents the statistical average difference / RMS difference computed over all corner reflectors imaged in all the lines flown on that particular flight. The average RCS RMS is 0.161 (0.648 dB) for HH, 0.175 (0.7 dB) for VV, and the average RMS HH-VV phase is 5.3°.

each of these methods derives estimates for u, v, w, z from the polarimetric covariance matrix, $C_{ij} =< O_i O_j^* >$, where the superscript $*$ denotes the complex conjugate. The quality of the cross-talk calibration depends both on the estimation method used as well as the details of the averaging of the polarimetric covariance matrix. We have considered two ways to average the polarimetric covariance matrix and apply the cross-talk parameters. In the first, we consider the parameters to be only a function of range, while the second method assumes the parameters may be scene dependent.

We first used Quegan's method (see Appendix A-B) to compute the cross-talk parameters as a function of range. For every line of constant range we compute the covariance matrix C^0 for a "stripe" of pixels that lie within 10 samples of the current range bin. We also computed the $HH-HV$ correlation in a 5 by 5 pixel box centered on each pixel and remove pixels where the correlation exceeds 0.2, similar to [13], since the Quegan algorithm requires that the true co-polarized / cross-polarized correlation be zero. We then use these covariance matrices to estimate the cross-talk parameters for each range-line. Hereafter, we will refer to this as the "stripe" method for computing the covariance matrix. In Figure 7 we plot an example of the cross-talk parameters as a function of range estimated using Quegan's method and the "stripe" method for the covariance computation. Before cross-talk calibration we see that the parameters are in the order of -15 dB, and the magnitude of the co-polarization leakage into the cross-polarizations is in the order of -30 dB[4].

However, we encountered some difficulties using the combined Quegan and "stripe" methods to estimate and correct for cross-talk. Most significantly, there are scenes where this method will produce such a poor estimate of α as to actually

[4]Derived from Eq. 12 neglecting co-pol cross-pol correlations.

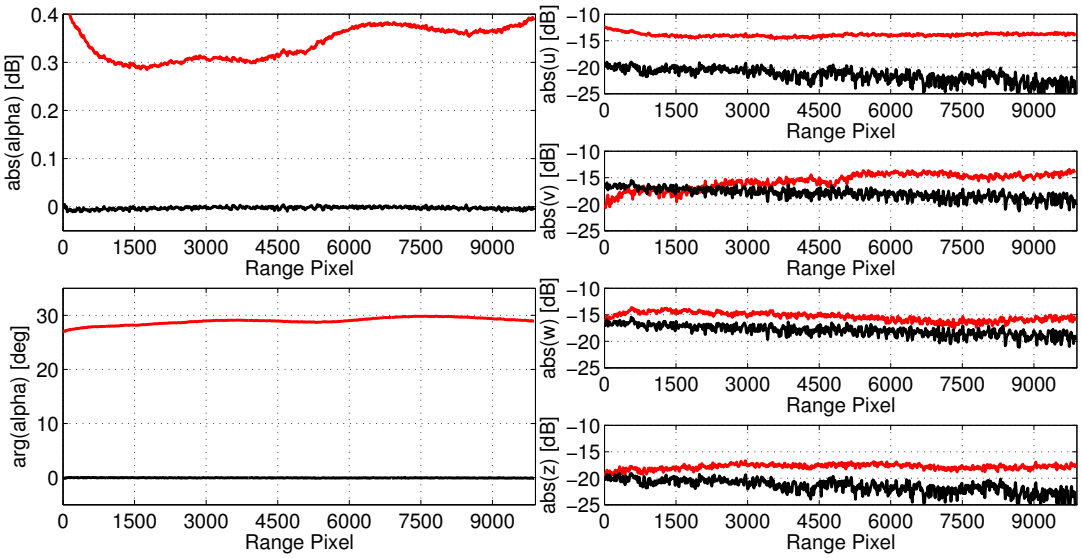

Fig. 7. Cross-talk parameters computed using Quegan's method from a covariance matrix generated using "stripes" in azimuth, plotted as a function of range. We plot the initial cross-talk estimates in red and the residual cross-talk remaining after cross-talk calibration in black. We see that the cross-talk parameters are all nearly -15 dB or smaller before cross-talk calibration. The estimates of residual cross-talk (black) are somewhat improved. We see that the residual α estimate is nearly 1 with almost zero phase, which means the cross-polarization channels have been well calibrated prior to cross-talk removal.

make the calibration worse. We observed this effect primarily in scenes that are dominated by ocean returns. To mitigate this issue we use a two-dimensional sliding window to average the covariance matrix as this would ensure that regions over an island are not impacted by the low entropy ocean scattering. Again, we mask out pixels where the $HH - HV$ correlation exceeds a threshold; we will refer to this as the "window" method.

Using Quegan's method and the window method to compute the cross-talk parameters results in estimates of the cross-talk parameters that vary strongly with the target. In Figure 8 we plot the z parameter for an agricultural scene as estimated using the Quegan (right) and the Ainsworth et al. (left) methods and a moving window of 201 pixels in range and 201 pixels in azimuth. We can clearly see that the plots on the right show sharp variations along field boundaries as the target type changes whereas the plots on the left do not show nearly as much variation or target-dependence. We find that the Ainsworth et al. method gives more consistent cross-talk estimates across changing targets and results in a calibration with significantly less residual cross-talk. In Figure 9 we plot the azimuth-averaged cross-talk parameters computed using the window method for the covariance matrix computation and both the Quegan method, Figure 9(a) and the the Ainsworth et al. method, Figure 9(b). In Figure 9(b) we show that the estimates of the cross-talk parameters are all on the order of -15 dB indicating leakage from the co-polarization into the cross-polarization in the order of -30 dB.

We suspect that part of the reason for the significantly lower residual cross-talk in the Ainsworth et al. method is due to its iterative nature. However, the assumptions of the Ainsworth et al. method are also less restrictive than those of the Quegan method. Based upon our observations that the cross-talk parameters are less dependent on the target type we think that the less restrictive assumptions are more physically correct. After cross-talk removal, residual cross-talk parameter estimates are generally in the order of -30 dB using the Ainsworth et al. method and -15 to -20 dB using the Quegan method. These correspond to about -60 dB and -30 to -40 dB co-polarization to cross-polarization leakage for the Ainsworth and Quegan methods, respectively. The Ainsworth et al. method combined with the sliding window for the covariance matrix computation has been adopted for standard UAVSAR product generation.

TABLE III
SUMMARY OF UAVSAR PERFORMANCE.

Parameter	Performance
Range resolution	2.534 m
Azimuth resolution	0.941 m
NESZ	-30 to -50 dB
RMS phase errors	5.3°
RMS calibration errors	0.7 dB
Polarization Leakage	< -30 dB

VI. CONCLUSION

We have shown that UAVSAR is a well calibrated platform for radiometric and polarimetric studies by performing radiometric and phase calibration using both point targets and distributed targets. The noise-equivalent-sigma-naught is less than -30 dB over the entire swath, and much better -40 to -55 dB in the near and mid-swath. Except for a hardware change, the NESZ performance has been very consistent over time. The geometric performance as assessed at corner reflectors has been very stable over time and across hardware configurations. We find the azimuth resolution of UAVSAR

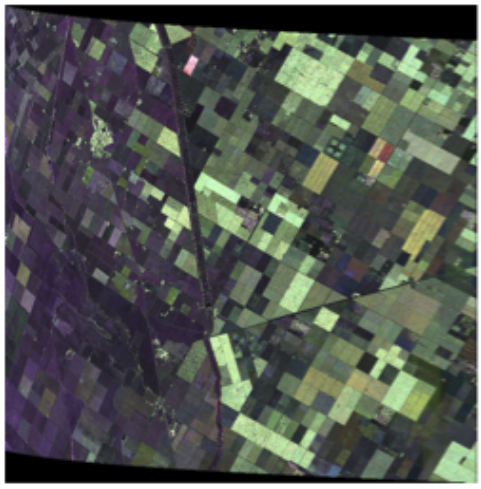

(a) Color-composite Image of San Joaquin Valley

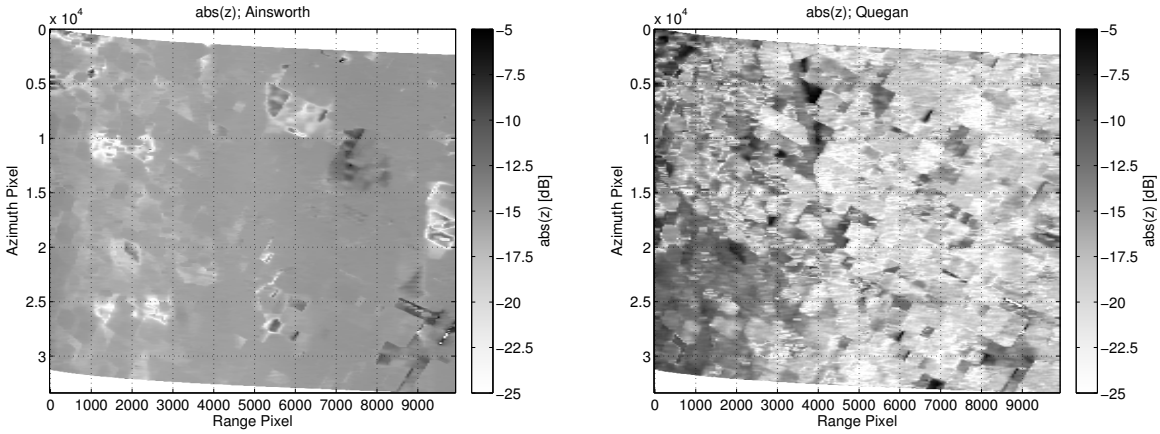

(b) abs(z) dB

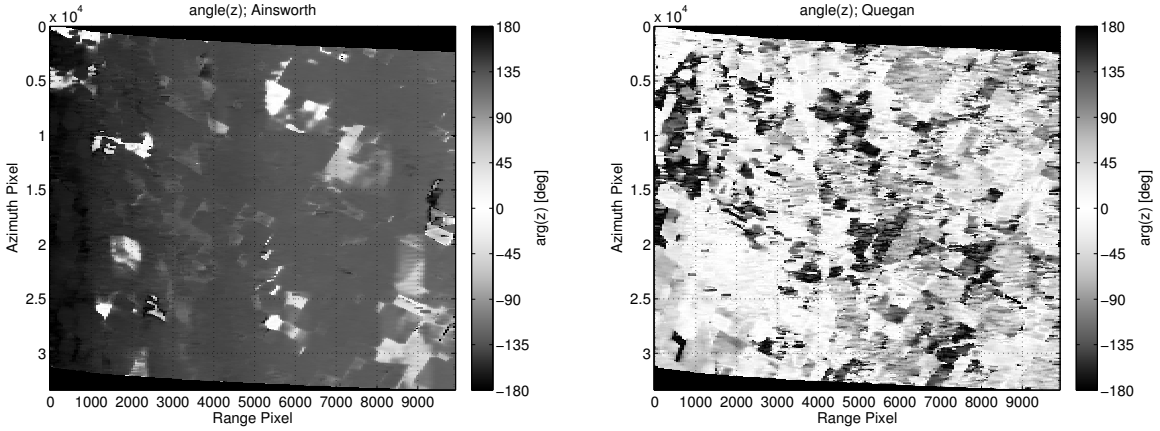

(c) arg(z) deg

Fig. 8. In 8(a) we plot a color-composite image of the San Joaquin Valley (Red=HH, Green=HV, Blue=VV); in 8(b) we plot the magitude (in dB) of the z parameter estimated using the Ainsworth et al. method (left) and Quegan's method (right); and in 8(c) we plot the phase (in degrees) of the z parameter. All images have azimuth as the vertical axis and range as the horizontal axis (near-range is on left side of each image). We see that the z parameter computed using the Quegan algorithm has large variations in amplitude and phase as the target changes, but that the parameter estimated using the Ainsworth et al. method is much smoother. Other u, v, w parameters (not plotted) show qualitatively similar features.

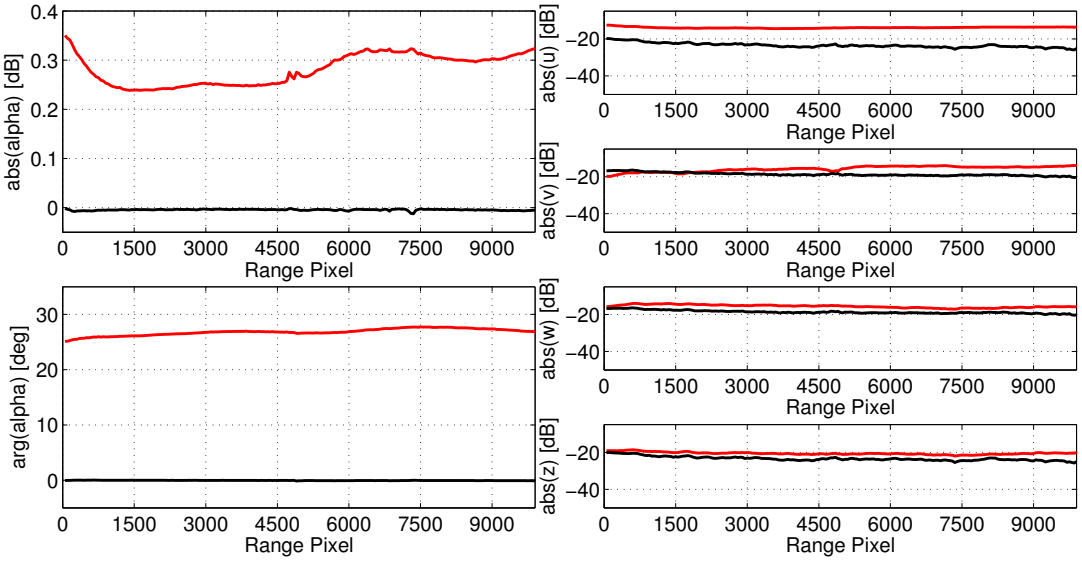

(a) Azimuth-averaged Quegan cross-talk parameters plotted as a function of range pixel

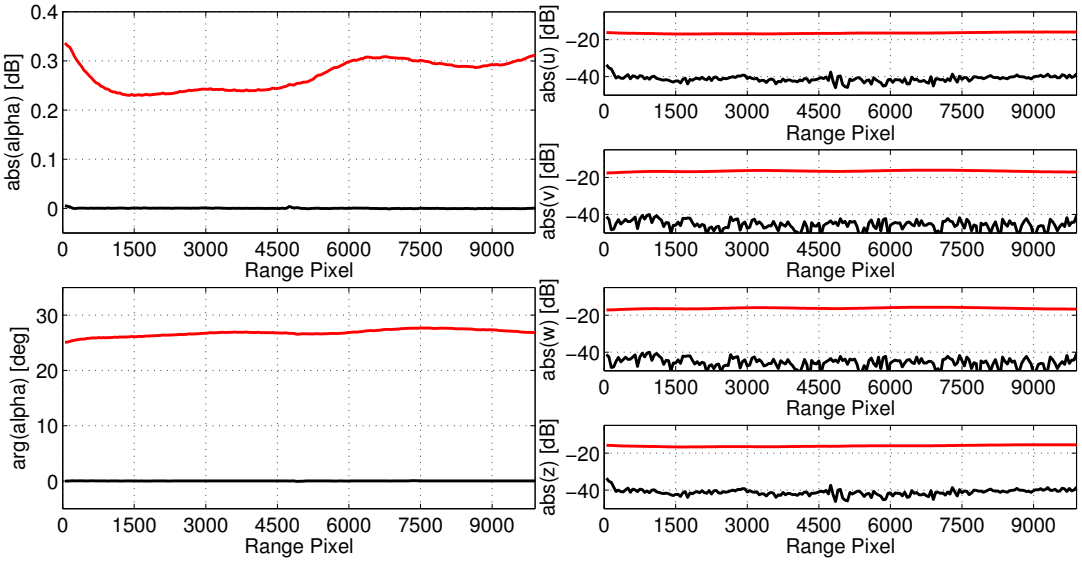

(b) Azimuth-averaged Ainsworth cross-talk parameters plotted as a function of range pixel

Fig. 9. Cross-talk parameters averaged in the azimuthal direction and plotted as a function of range, computed using Quegan's method (a) and the Ainsworth et al. method (b) from a covariance matrix generated using a moving window of 201x201 pixels. We plot the initial cross-talk estimates in red and the residual cross-talk remaining after cross-talk calibration in black. We see that the estimated residual cross-talk in (b) is significantly less than that in (a). These parameters were estimated from the same scene as in Figure 7.

to be 0.94 meters and the range resolution to be 2.53 meters, in fairly good agreement with expected values. Our analyses show that UAVSAR is radiometrically calibrated to better than 1 dB in calibration bias, 0.7 dB in residual RMS calibration error, the phase calibration is about $5.3°$, the co-polarization channel imbalance error is 0.04 (linear units), and the leakage of the co-polarizations into the cross-polarizations is on the order of -30 dB. We explored two methods of estimating the cross-talk between the H-polarization and V-polarization channels based on backscatter from distributed targets, the methods of Quegan [9] and Ainsworth et al. [8]. We find the method of Ainsworth et al. gives more stable cross-talk estimates.

ACKNOWLEDGEMENTS

This work was performed under contract with the National Aeronautics and Space Administration at the Jet Propulsion Laboratory, California Institute of Technology. Copyright 2014 California Institute of Technology. Government sponsorship acknowledged.

APPENDIX A
ESTIMATION OF CROSS-TALK PARAMETERS

In its most general form, the polarimetric covariance matrix can be written as

$$\mathbf{C} = \left\langle \begin{pmatrix} S_{hh}S_{hh}^* & S_{hh}S_{vh}^* & S_{hh}S_{hv}^* & S_{hh}S_{vv}^* \\ S_{vh}S_{hh}^* & S_{vh}S_{vh}^* & S_{vh}S_{hv}^* & S_{vh}S_{vv}^* \\ S_{hv}S_{hh}^* & S_{hv}S_{vh}^* & S_{hv}S_{hv}^* & S_{hv}S_{vv}^* \\ S_{vv}S_{hh}^* & S_{vv}S_{vh}^* & S_{vv}S_{hv}^* & S_{vv}S_{vv}^* \end{pmatrix} \right\rangle, \tag{16}$$

which is a Hermetian matrix. Hereafter we denote elements of this matrix as C_{ij} for row i and column j. The Quegan method assumes the following "true" covariance matrix:

$$\mathbf{C}_Q = \left\langle \begin{pmatrix} \sigma_{hhhh} & 0 & 0 & \sigma_{hhvv} \\ 0 & \beta & \beta & 0 \\ 0 & \beta & \beta & 0 \\ \sigma_{hhvv}^* & 0 & 0 & \sigma_{vvvv} \end{pmatrix} \right\rangle, \tag{17}$$

and the Ainsworth et al. method assumes

$$\mathbf{C}_A = \left\langle \begin{pmatrix} \sigma_{hhhh} & A^* & A^* & \sigma_{hhvv} \\ A & \beta & \beta' & B \\ A & \beta' & \beta & B \\ \sigma_{hhvv}^* & B^* & B^* & \sigma_{vvvv} \end{pmatrix} \right\rangle. \tag{18}$$

The two major differences are that the Quegan method uses a symmetrized (i.e. hv=vh) truth covariance matrix and the Quegan method forces the co-polarization to cross-polarization (A, B) covariance matrix elements to be zero.

A. Ainsworth Parameter Estimation

In our implementation of the Ainsworth et al. algorithm, the α, A, B estimates are given by

$$\alpha = \frac{C_{23}}{|C_{23}|}\sqrt{|\frac{C_{22}}{C_{33}}|}, \tag{19}$$

$$A = 0.5(C_{31} + C_{21}), \tag{20}$$

$$B = 0.5(C_{34} + C_{24}), \tag{21}$$

and u, v, w, z are given by the solution to the linear system of equations

$$\begin{bmatrix} \Re[\boldsymbol{\zeta}+\boldsymbol{\tau}] & -\Im(\boldsymbol{\zeta}-\boldsymbol{\tau}) \\ \Im[\boldsymbol{\zeta}+\boldsymbol{\tau}] & \Re(\boldsymbol{\zeta}-\boldsymbol{\tau}) \end{bmatrix} \begin{bmatrix} \Re[\boldsymbol{\delta}] \\ \Im[\boldsymbol{\delta}] \end{bmatrix} = \begin{bmatrix} \Re[\mathbf{X}] \\ \Im[\mathbf{X}] \end{bmatrix}, \tag{22}$$

where

$$\boldsymbol{\zeta} = \begin{bmatrix} 0 & 0 & C_{41} & C_{11} \\ C_{11} & C_{41} & 0 & 0 \\ 0 & 0 & C_{44} & C_{14} \\ C_{14} & C_{44} & 0 & 0 \end{bmatrix},$$

$$\boldsymbol{\tau} = \begin{bmatrix} 0 & C_{33} & C_{32} & 0 \\ 0 & C_{23} & C_{22} & 0 \\ C_{33} & 0 & 0 & C_{32} \\ C_{23} & 0 & 0 & C_{22} \end{bmatrix},$$

$$\mathbf{X} = \begin{bmatrix} C_{31} - A \\ C_{21} - A \\ C_{34} - B \\ C_{24} - B \end{bmatrix} \tag{23}$$

$\boldsymbol{\delta} = [u, v, w, z]^T$, and $(\Re, \Im)$ denote the real and imaginary parts, respectively [8]. The decomposition into $\boldsymbol{\zeta}$ and $\boldsymbol{\tau}$ is required as the complex system of equations involves both (u, v, w, z) and their complex conjugates. When factoring the system of equations into real and imaginary parts, all terms that have complex conjugates of (u, v, w, z) are accounted by $\boldsymbol{\tau}$ matrix, hence the somewhat odd appearance of (22).

To compute the cross-talk parameters from the covariance matrix of Ainsworth et al. we use an iterative algorithm outlined below:

Compute $\mathbf{C}^0$ in window
$\gamma = 100$
$TOL = 1E-8$
$i_{iter} = 0$
$u = v = w = z = 0$
Estimate α from $\mathbf{C}^0$ Using (19)
while $\gamma > TOL$ and $i_{iter} < 12$ **do**
  $i_{iter} = i_{iter} + 1$
  Compute $\boldsymbol{\Sigma}_i$ using (u, v, w, z, α)
  Compute $\mathbf{C}^i = \boldsymbol{\Sigma}_i \mathbf{C}^0 \boldsymbol{\Sigma}_i^\dagger$
  Estimate A, B from $\mathbf{C}^i$
  Estimate $(u_i, v_i, w_i, z_i, \alpha_i)$ from $\mathbf{C}^i$, A, B (from solution of (22) and (19))
  $u \leftarrow u + u_i/\sqrt{\alpha}$
  $v \leftarrow v + v_i/\sqrt{\alpha}$
  $w \leftarrow w + w_i\sqrt{\alpha}$
  $z \leftarrow z + z_i\sqrt{\alpha}$
  $\alpha \leftarrow \alpha\alpha_i$
  $\gamma = \max(|u_i|, |v_i|, |w_i|, |z_i|)$
end while

B. Quegan Parameter Estimation

We use an algorithm similar to methods described in [9]. From the covariance matrix, we estimate the cross-talk parameters as

$$\begin{aligned} u &= (C_{44}C_{21} - C_{41}C_{24})/\Delta, \\ v &= (C_{11}C_{24} - C_{21}C_{14})/\Delta, \\ z &= (C_{44}C_{31} - C_{41}C_{34})/\Delta, \\ w &= (C_{11}C_{34} - C_{31}C_{14})/\Delta, \end{aligned} \tag{24}$$

where $\Delta = C_{11}C_{44} - |C_{14}|^2$. Note that these equations were derived in [9] by neglecting terms of second order or higher in (u, v, w, z). The cross-polarization channel imbalance is estimated as

$$\alpha = \frac{|\alpha_1\alpha_2| - 1 + \sqrt{(|\alpha_1\alpha_2| - 1)^2 + 4 + |\alpha_2|^2}}{2|\alpha_2|}\frac{\alpha_1}{|\alpha_1|}, \tag{25}$$

where

$$\begin{aligned} \alpha_1 &= \frac{C_{22} - uC_{12} - vC_{42}}{X}, \\ \alpha_2 &= \frac{X*}{C_{33} - z^*C_{31} - w^*C_{34}}, \\ X &= C_{32} - zC_{12} - wC_{42}. \end{aligned} \tag{26}$$

With these estimates we can compute the calibration matrix, $\boldsymbol{\Sigma}$.

REFERENCES

[1] S. Hensley, H. Zebker, C. Jones, T. Michel, R. Muellerschoen, and B. Chapman, "First deformation results using the NASA/JPL UAVSAR instrument," in *Synthetic Aperture Radar, 2009. APSAR 2009. 2nd Asian-Pacific Conference on*, 2009, pp. 1051–1055.

[2] J. Lee, B. Strovers, and V. Lin, "C-20A/GIII precision autopilot development in support of NASAs UAVSAR program," in *Proceeding of the NASA Science Technology Conference 2007*. NASA, 2007.

[3] R. R. Bonkowski, C. R. Lubitz, and C. E. Schensted, "Studies in Radar Cross-Sections - VI. Cross-sections of corner reflectors and other multiple scatterers at microwave frequencies," University of Michigan Radiation Laboratory, http://hdl.handle.net/2027.42/21139, Tech. Rep., October 1953.

[4] S. Hensley, S. Oveisgharan, S. Saatchi, M. Simard, R. Ahmed, and Z. Haddad, "An error model for biomass estimates derived from polarimetric radar backscatter," *Geoscience and Remote Sensing, IEEE Transactions on*, vol. 52, no. 7, pp. 4065–4082, July 2014.

[5] J. van Zyl, C. F. Burnette, H. A. Zebker, A. Freeman, and J. Holt, "Polcal user's manual," Jet Propulsion Laboratory, Tech. Rep., August 1992.

[6] A. Freeman, Y. Shen, and C. Werner, "Polarimetric SAR calibration experiment using active radar calibrators," *Geoscience and Remote Sensing, IEEE Transactions on*, vol. 28, no. 2, pp. 224 –240, March 1990.

[7] A. Freeman, "SAR calibration: an overview," *Geoscience and Remote Sensing, IEEE Transactions on*, vol. 30, no. 6, pp. 1107 –1121, November 1992.

[8] T. Ainsworth, L. Ferro-Famil, and J.-S. Lee, "Orientation angle preserving a posteriori polarimetric SAR calibration," *IEEE Transactions on Geoscience and Remote Sensing*, vol. 44, no. 4, pp. 994–1003, April 2006.

[9] S. Quegan, "A unified algorithm for phase and cross-talk calibration of polarimetric data-theory and observations," *IEEE Transactions on Geoscience and Remote Sensing*, vol. 32, no. 1, pp. 89–99, January 1994.

[10] H. A. Zebker, J. van Zyl, and D. N. Held, "Imaging radar polarimetry from wave synthesis," *J. Geophys. Res.*, vol. 92, 1987. [Online]. Available: http://dx.doi.org/10.1029/JB092iB01p00683

[11] J. van Zyl, H. A. Zebker, and C. Elachi, "Imaging radar polarization signatures: Theory and observation," *Radio Sci.*, vol. 22, 1987. [Online]. Available: http://dx.doi.org/10.1029/RS022i004p00529

[12] S. Durden, J. van Zyl, and H. Zebker, "Modeling and observation of the radar polarization signature of forested areas," *Geoscience and Remote Sensing, IEEE Transactions on*, vol. 27, no. 3, pp. 290–301, May 1989.

[13] H. Kimura, T. Mizuno, K. Papathanassiou, and I. Hajnsek, "Improvement of polarimetric SAR calibration based on the Quegan algorithm," in *Geoscience and Remote Sensing Symposium, 2004. IGARSS '04. Proceedings. 2004 IEEE International*, vol. 1, September 2004, pp. 184–187.